# Levetiracetam Modulates Brain Metabolic Networks and Transcriptomic Signatures in the 5XFAD Mouse Model of Alzheimer's disease.

Charles P. Burton[1], Evgeny J. Chumin[1,2], Alyssa Y. Collins[1], Scott A. Persohn[1], Kristen D. Onos[3], Ravi S. Pandey[4], Sara K. Quinney[5], and Paul R. Territo[1,5]

Affiliations:

[1] Stark Neurosciences Research Institute, Indiana University School of Medicine, Indianapolis IN 46202 USA

[2] Department of Radiology and Imaging Sciences, Indiana University School of Medicine, Indianapolis IN 46202

[3] The Jackson Laboratory, Bar Harbor, ME 04609

[4] The Jackson Laboratory for Genomic Medicine, Farmington, CT 06032

[5] Department of Medicine, Division of Clinical Pharmacology, Indiana University School of Medicine, Indianapolis IN 46202 USA

**CORRESPONDING AUTHOR:**

Paul R. Territo, Ph.D.

1345 West 16th Street, BRTC 308

Indianapolis, Indiana 46202

pterrito@iu.edu

**SHORT TITLE:** Levetiracetam Modulates Connectomics and Transcriptomics in 5XFAD Mice

**KEYWORDS:** Levetiracetam; Alzheimer's disease; 5XFAD; Connectomics

**ABSTRACT:**

*INTRODUCTION:* Subcritical epileptiform activity is associated with impaired cognitive function and is commonly seen in patients with Alzheimer's disease (AD). The anti-convulsant, levetiracetam (LEV), is currently being evaluated in clinical trials for its ability to reduce epileptiform activity and improve cognitive function in AD. The purpose of the current study was to apply pharmacokinetics (PK), network analysis of medical imaging, gene transcriptomics, and PK/PD modeling to a cohort of amyloidogenic mice to establish how LEV restores or drives alterations in the brain networks of mice in a dose-dependent basis using the rigorous preclinical pipeline of the MODEL-AD Preclinical Testing Core.

*METHODS:* Chronic LEV was administered to 5XFAD mice of both sexes for 3 months based on allometrically scaled clinical dose levels from PK models. Data collection and analysis consisted of a multi-modal approach utilizing $^{18}$F-FDG PET/MRI imaging and analysis, transcriptomic analyses, and PK/PD modeling.

*RESULTS:* Pharmacokinetics of LEV showed a sex and dose dependence in $C_{max}$, CL/F, and $AUC_{0-\infty}$, with simulations used to estimate dose regimens. Chronic dosing at 10, 30, and 56 mg/kg, showed $^{18}$F-FDG specific regional differences in brain uptake, and in whole brain covariance measures such as clustering coefficient, degree, network density, and connection strength (i.e. positive and negative). In addition, transcriptomic analysis via nanoString showed dose-dependent changes in gene expression in pathways consistent $^{18}$F-FDG uptake and network changes, and PK/PD modeling showed a concentration dependence for key genes, but not for network covariance modeling.

*DISCUSSION:* This study represents the first report detailing the relationships of metabolic covariance and transcriptomic network changes resulting from LEV administration in 5XFAD mice. Overall, our results highlight non-linear kinetics based on dose and sex, where gene expression analysis demonstrated LEV dose- and concentration- dependent changes, along with cerebral metabolism, and/or cerebral homeostatic mechanisms relevant to human AD, which aligned closely with network covariance analysis of $^{18}$F-FDG images. Collectively, this study show cases the value of a multimodal connectomic, transcriptomic, and pharmacokinetic approach to further investigate dose dependent relationships in preclinical studies, with translational value towards informing clinical study design.

54 **INTRODUCTION**

55 Subclinical epileptiform activity is commonplace in both mouse models of Alzheimer's Disease (AD) and
56 in the clinic (Minkeviciene et al., 2009;Vossel et al., 2016). Recent work has shown that sustained
57 expression of the calcium binding protein, calbindin-$D_{28K}$, buffers cytosolic calcium in mouse models of
58 AD, while healthy controls showed decreased expression with age in subicular dendrites, thus forming a
59 molecular basis of epileptiform activity in models of AD (Stafstrom, 2005;Angulo et al., 2020). Additional
60 work has reported spike wave discharge activity in the 5XFAD mouse of model of AD, which is consistent
61 with human AD epileptiform activity, where hippocampal hyper-excitability has been observed in human
62 *APOE*$^{E4/E4}$ carriers (Tran et al., 2017). Importantly, this activity has been shown to localize to β-amyloid
63 (Aβ) plaques, where neuronal dysregulation is thought to result from impaired synaptic inhibition, thus
64 driving aberrant excitatory activity. Neurons distal to the plaques show abnormally low spike wave
65 discharge activity (Palop et al., 2007), suggesting that Aβ plaque load may play an important role in
66 epileptiform formation. Provided this, anti-epileptic drugs have been considered as a possible treatment
67 paradigm and are hypothesized to attenuate synchronized hyperactivity in patients with AD (Palop, 2009).
68 One drug in particular, Levetiracetam (LEV), received FDA approval in 2000 for the treatment of seizures
69 and epilepsy in adults and adolescents (Kumar et al., 2023). Recent clinical trials administering LEV in
70 AD patients have found improved cognitive function in patients with epileptiform activity (Vossel et al.,
71 2021). In humanized amyloid precursor protein (*hAPP)* mice, LEV significantly reduced epileptiform
72 activity in a dose-dependent manner and halted disease progression (Sanchez et al., 2012). Combined,
73 these data suggest that LEV treatment may be efficacious in attenuating disease progression in 5XFAD
74 mice that overexpress Aβ and suggest that prophylactic treatment with LEV may provide experimental
75 evidence as a treatment for late onset AD (LOAD) [6].

76 Clinically, hyper-excitability has been associated with seizures in AD patients (Lippa et al.,
77 2010;Vossel et al., 2016;Toniolo et al., 2020). This phenomenon is also observed in AD mouse models
78 such as 5XFAD and *APP/PS1* (Schneider et al., 2014;Klee et al., 2020). LEV's acute administration in
79 amyloid mouse models has shown attenuation of abnormal spike wave activity (Klee et al., 2020), while
80 chronic treatment via continuous mini-pump infusion has been associated with the reversal of synaptic

loss and behavioral impairment in *hAPP* mice (Sanchez et al., 2012). However, prior preclinical studies have not fully characterized the pharmacokinetics (PK) of LEV and its impact on gene transcriptomic and brain metabolic network alterations that are crucial for predicting the observed nonlinear dose efficacy in clinical studies. Notably, single-daily dosing of LEV may not maintain exposure levels, and could result in elevated $C_{min}/C_{max}$ ratios, thus reducing drug effectiveness and potentially resulting in $C_{max}$ dependent toxicities.

Although the precise mechanism of action of LEV in AD is not fully understood, it is known to modulate the release of synaptic neurotransmitters by antagonizing SV2A receptors (Lynch et al., 2004;Kumar et al., 2023). Moreover, neuromodulation is thought to occur through the inhibition of presynaptic calcium channels, reducing impulse conductivity and thus enhancing the preferential transmission of low-frequency signals (García-Pérez et al., 2015). During the repurposing of LEV for use in mild cognitive impairment (MCI) studies, a nonlinear dose-dependent response curve was observed in the form of an inverted paraboloid (Bakker et al., 2012;Bakker et al., 2015;Magalhães et al., 2015;Musaeus et al., 2017). A study with control and MCI participants imaged with functional magnetic resonance imaging (MRI) while performing a memory task revealed that the low (62.5 mg twice daily (BID)) and moderate (125 mg BID) doses of LEV restored normal hippocampal activity in the dentate gyrus and CA3 regions. However, this effectiveness was not observed in the highest (250 mg BID) dose studied, suggesting a resurgence in nonequilibrium synchronization in the hippocampus (Bakker et al., 2012).

Previous work from our lab has explored the pharmacokinetic (PK) and pharmacodynamic (PD) relationships of LEV in a mouse model of AD that could be used to better predict clinical efficacy (Onos et al., 2022). We evaluated LEV using the validated pipeline of the Model Organism Development and Evaluation for Late Onset Alzheimer's Disease (MODEL-AD) Preclinical Testing Core (PTC), where we determined the PK of LEV in the 5XFAD mouse model, permitting the determination of dose, frequency, and duration for chronic studies. We performed PD assessment followed chronic administration, where $^{18}$F-AV45 and $^{18}$F-FDG PET/MRI showed dose-dependent reduction in amyloid deposition and glucose uptake across imaging cohorts. Additional sex and dose dependencies were seen in nanoString

108 estimates of transcriptional changes, which underpin the PD changes. Though these results showed
109 significant alterations in PK and PD as a function of treatment, methods to elucidate how LEV modified
110 gene and associated brain networks and how this related to blood and brain drug concentrations (i.e.
111 PK/PD) was not investigated (Onos et al., 2022).

112 Recent work from our group has applied a metabolic network covariance modeling approach in
113 the 5XFAD model across lifespan (i.e. 4, 6, and 12 mos) (Chumin et al., 2023). This work permits the
114 interrogation of network changes at the whole brain and sub-network levels, allowing greater insights into
115 the network changes that occur with disease progression. Here, we applied this method to investigate
116 LEV treatment and subsequent interregional metabolic changes in 5XFAD mice of both sexes. Our goal
117 was to establish a clear dose/concentration-dependent relationship of LEV treatment in conjunction with
118 alterations in brain metabolic uptake network and gene expression to better predict clinical efficacy, which
119 is not currently possible using traditional analytical approaches.

120

121 **METHODS**

122 All studies adhered to the ARRIVE guidelines and received approval from the Institutional Animal Use
123 and Care Committees (IACUC at their respective locations).

124

125 *Housing conditions and cohort generation at Indiana University (IU):*

126 Adult male 5XFAD mice, female 5XFAD mice, and non-transgenic WT controls were produced through
127 a breeding program at Indiana University (IU). This involved mating male 5XFAD mice (JAX MMRRC
128 stock #:34848) with female C57BL6/J mice (JAX MMRRC stock #:000664). The animals were
129 accommodated in cages, with up to five mice per cage, and were provided with SaniChip bedding.
130 Throughout the dosing studies, the mice continued to reside in group housing arrangements. The colony
131 room maintained a 12:12 Light:Dark schedule, with lights turning on at 6:00 am. One cohort was studied,
132 designed for the endpoint of $^{18}$F-FDG PET.

133

134 *Housing conditions and cohort generation at The Jackson Laboratory (JAX):*

135 Adult male 5XFAD mice, female 5XFAD mice, and non-transgenic WT controls were bred at JAX using
136 the same breeding methods as those employed at IU. Initially, mice were accommodated in duplex cages
137 with pine bedding, allowing up to five mice per side. The colony room adhered to a 12:12 Light:Dark
138 schedule. For chronic dosing studies, each treatment group consisted of approximately 10-15 mice per
139 sex. To ensure randomization, both treatment and sex were randomized across two cohorts, which were
140 staggered by a 4-week interval. Each cohort was comprised of 5-8 mice per sex per treatment. One week
141 prior to the beginning of the study, the mice were individually housed and subsequently transported to a
142 colony room located adjacent to the behavioral testing facility.
143
144 *Levetiracetam Pharmacokinetic Studies:*
145 *In vivo* PK sampling for LEV was initially carried out at JAX following dosing and serial sampling in 6-
146 month-old male and female 5XFAD mice. LEV (Sigma # L8668-100mg; Lot # 051M4742V) was dissolved
147 in sterile saline (vehicle). Mice (with n=3 dose per sex) were administered doses of 10, 30, and 100 mg/kg
148 (dose volume 10 mL/kg) via oral gavage as described previously (Onos et al., 2022). Serial plasma
149 samples were collected via the tail vein prior to dosing and at 0.25, 0.5, 1, 2, 4, 6, and 24 hours post-
150 dosing. Mice were euthanized at 24 hours, brains excised, frozen using dry ice, and stored at -80°C.
151 Samples were shipped to IU for quantification of LEV and PK analysis per our previous work (Onos et
152 al., 2022).
153
154 *Levetiracetam Quantification:*
155 LEV and etiracetam (ECA) concentrations were determined in plasma and brain samples using
156 LC/MS/MS, with temazepam as an internal standard as described previously (Onos et al., 2022).
157 Standard curves were established over a concentration range of 0.3-30000 ng/mL for plasma samples
158 and 0.8-800 ng/g for brain homogenate samples. The inter-day precision ranged from 5.3% to 15.4% for
159 LEV and 10.7% to 17.0% for ECA, while the inter-day accuracy ranged from 88.1% to 108.0% for LEV
160 and 88.4% to 103.0% for ECA.
161

162 *Pharmacokinetic Modeling:*

163 PK parameters were initially calculated using standard noncompartmental analysis (NCA) performed with
164 WinNonlin (Phoenix 64, build 8.0.0.3176), as we have previously described (Onos et al., 2022). To
165 estimate chronic exposure, a population pharmacokinetic analysis was conducted in Monolix 2023R1
166 (Lixoft). Apparent clearance (CL/F) and volume (V/F) were allometrically scaled to weight with fixed
167 coefficients of 0.75 and 1.0, respectively. Dose and sex were tested as covariates on CL/F and V/F.
168 Model and covariate selection was based on reduction of objective function value of at least 3.84 ($\chi^2$,
169 $p<0.05$), goodness of fit plots, covariate vs. eta plots, and visual predictive checks. Clearance for
170 individual mice following chronic treatment with levetiracetam was calculated in Sumlx (2023R1, Lixoft)
171 population estimates (thetas), and area under the concentration time (AUC) calculated as dose-
172 normalized clearance. Data were analyzed and plotted in R version 4.3.0 (Team, 2023).

173

174 *Magnetic Resonance Imaging*

175 High-contrast gray matter images were acquired 2 days prior to PET imaging, where mice were induced
176 with 5% isoflurane in medical oxygen, placed on the head coil, and anesthesia was maintained with 1–
177 3% isoflurane for scan duration. High-resolution T2-weighted (T2W) MRI images were acquired using a
178 3T Siemens Prisma clinical MRI scanner outfitted with a dedicated 4-channel mouse head coil and bed
179 system (RAPID MR, Columbus, OH, United States) per our previous work (Oblak et al., 2021;Onos et
180 al., 2022).

181

182 *In vivo PET Imaging and Analysis*

183 Regional brain glycolytic metabolism was monitored using 2-$^{18}$F-fluoro-2-deoxy-d-glucose ($^{18}$F-FDG),
184 where clinical unit doses ranging from 185 MBq (5 mCi) were purchased from PETNet Indiana (PETNET
185 Solutions Inc.). In all cases, mice were fasted for a minimum of 12 h prior to tracer administration. Mice
186 were injected IP with 3.7–11.1 MBq (100–300 uCi) with $^{18}$F-FDG and allowed 30 min of uptake in an
187 isothermal cage. For imaging, mice were then anesthetized with 5% isoflurane gas and maintained at
188 with 1–3% isoflurane per our previous work (Oblak et al., 2021;Onos et al., 2022), and scanned on the

189 IndyPET3 (Rouzes et al., 2004) scanner for 15 min. Images were calibrated, and decay- and scatter-
190 corrected PET images were reconstructed into a single-static image volume according to our previous
191 work (Oblak et al., 2021;Onos et al., 2022). All images were co-registered using a rigid-body mutual
192 information-based normalized entropy algorithm with 9° of freedom and mapped to stereotactic mouse
193 brain coordinates according to our previous work (Oblak et al., 2021;Onos et al., 2022). Post-registration,
194 56 regions were extracted via Paxinos and Franklin's 2007 brain atlas and averaged to yield 28 bilateral
195 regions (Paxinos and Keith B. J. Franklin, 2007). Standardized Uptake Value Ratios (SUVr; normalized
196 to cerebellum) were computed for all regions relative to cerebellum, and principal component analysis
197 was performed to provide data reduction for all PET regions. Consensus regions which explained 80%
198 of the variance observed across all regions studied were selected for regional interrogation via MANOVA,
199 correcting for multiple comparisons with a Bonferroni correction. To assess whole brain and sub-network
200 changes in $^{18}$F-FDG images, metabolic covariance analysis was conducted according to our recent work
201 and open source tools (Chumin et al., 2023). Pearson's correlation between z-scores of region pairs was
202 calculated for all pairwise interactions within each cohort to generate a covariance adjacency matrix (see
203 Figures. 3, 5-7). To assess metabolic network characteristics, a correlation threshold of $p<0.05$ was
204 applied to adjacency matrices, with only significant edges surviving (Figure 3). Multiple alpha values were
205 tested, but thresholds more restrictive than $p<0.05$ yielded graphs too sparse for meaningful analysis.
206 The nodal degree, positive strength, negative strength, and clustering coefficient was computed for every
207 brain region and the global distribution of nodal characteristics were compared across sex and treatment
208 using 2-sample Kolmogorov-Smirnov (KS) tests. To evaluate the sub-network modules, littermate control
209 (WT) community partitions were generated via multi-resolution consensus clustering (MRCC) analysis
210 (Jeub et al., 2018) and imposed on comparison groups. In sex comparisons, male littermate control
211 partitions were used. Mean metabolic SUVr were compared between like communities via ANOVA, with
212 a Bonferroni correction.
213
214 *Drug Administration for Chronic Studies:*

215 Mice were weighed daily and received oral gavage of LEV (SelleckChem # S1356, bulk lot # S135602)
216 dissolved in sterile saline twice daily (BID) for 3 months. LEV was administered between 7:00 am – 9:00
217 am and 3:00 pm – 5:00 pm, with a dose volume of 10 mL/kg. In all cases, LEV was formulated in sterile
218 saline weekly, and vials were blinded (i.e. A, B, C, and D (JAX) or Blue, Red, Yellow, and Green (IU)) in
219 accordance with ARRIVE guidelines (Percie du Sert et al., 2020). Drug stability was determined by IU
220 Clinical Pharmacology Analytical Core (CPAC) and was shown to be stable in the final formulation for a
221 one-week period. Throughout the chronic dosing period, animals were closely monitored for potential
222 signs of toxicity or drug-related side effects, where the attrition was very low (n = 3). This was not specific
223 to a dose level and occurred either due to dermatitis or lung puncture during oral gavage.
224
225 *Terminal Tissue Collection:*
226 Upon study completion plasma and brain tissue samples were collected from the subjects under
227 isoflurane anesthesia 30 min after the final LEV dose. Bioanalytical analysis was conducted via CPAC
228 for terminal plasma and the right brain hemisphere to confirm PK data. For transcriptional profiling,
229 homogenates from the left hemispheres were quantified using a customized nanoString nCounter®
230 Mouse AD panel designed to identify changes in gene expression associated with clinical LOAD.
231 Differential gene expression was assessed with consideration of genotype, sex, and treatment per our
232 previous work (Onos et al., 2022).
233
234 *nanoString Gene Expression Profiling and Analysis*
235 Methods for this assay have been published previously (Onos et al., 2022). Data were analyzed with the
236 use of QIAGEN IPA (QIAGEN Inc., https://digitalinsights.qiagen.com/IPA).
237
238 *Rigor and Reproducibility:*
239 During study execution and throughout data analysis, all technicians adhered to the ARRIVE guidelines
240 (Percie du Sert et al., 2020) and were unaware of the genotype and drug dosage information.
241

242 **RESULTS**

243 *Population Pharmacokinetics*

244 LEV concentration-time data fit a 1-compartment first order absorption model (Figure 1). After accounting
245 for weight, dose (but not sex) was found to be a significant covariate on oral clearance (CL/F) and
246 apparent volume of distribution (V/F), as indicated by reduced objective function value and improved
247 covariate vs. $\eta$ plots. As shown in **Figure 1B**, the predicted AUCs were significantly correlated with 0.5
248 hour plasma concentrations following twice-daily dosing of levetiracetam in mice housed at JAX ($p<0.001$,
249 $R^2=0.71$)

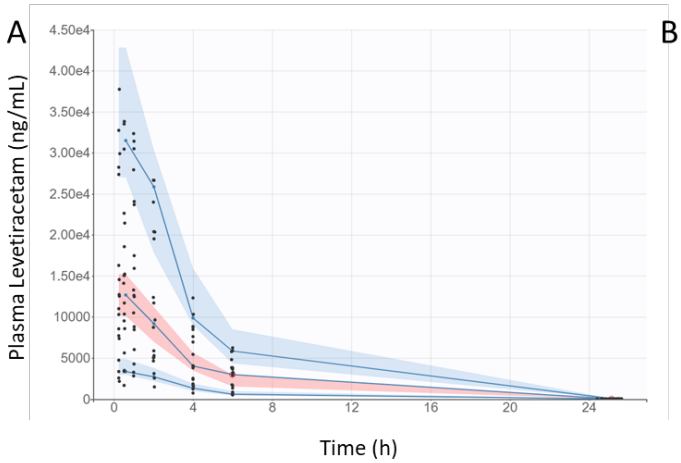


B

| Parameter | Estimate±SE (RSE%) |
|---|---|
| ka ($h^{-1}$) | 4.94 ± 0.67 (13.6) |
| V/F (L) | 0.039 ± 0.005 (11.8) |
| β, dose on V/F | 0.0054 ± 0.0019 (35.8) |
| CL/F (L/h) | 0.013 ± 0.0015 (11.3) |
| β, dose on CL/F | 0.0061 ± 0.0019 (30.4) |
| Random Effects | |
| $\omega_{ka}$ | 0.36 ± 0.14 (39.5) |
| $\omega_{V/F}$ | 0.3 0 ± 0.06 (19.6) |
| $\omega_{CL/F}$ | 0.30 ± 0.05 (18.2) |
| Additive error | 20.96 ± 3.92 (18.7) |
| Proportional error | 0.16 ± 0.016 (9.64) |
| Correlation V/F ~ CL/F | 0.7 ± 0.16 (22.3) |

**Figure 1.** Levetiracetam pharmacokinetics: (A) Visual predictive check demonstrates reasonable fit of population pharmacokinetic model to data. Points indicate individual observed data, solid lines represent median, 5th, and 95th percentiles of observed data, pink shaded area indicates 90% prediction interval of the median, blue shaded areas indicated 90% prediction intervals of the 5th and 95th percentiles of predicted data. (B) Final pharmacokinetic parameter estimates for population model of levetiracetam.

250 *General Linear Modeling of Brain $^{18}$F-FDG PET*

251 In chronic LEV-treated 5XFAD mice of both sexes, quantitative analysis of $^{18}$F-FDG PET uptake across
252 different dosage levels was performed after normalizing regional data with a standard uptake value ratio
253 (SUVr) to the cerebellum (Oblak et al., 2021;Onos et al., 2022). Using principal component analysis
254 (PCA), twelve out of the twenty-seven studied regions that consistently explained 80% of the variance in
255 $^{18}$F-FDG uptake between and within cohorts were identified (see Figure 2). In this model system, dynamic
256 range was determined to have a 1.5-fold difference in $^{18}$F-FDG uptake between WT and 5XFAD mice
257 (Oblak et al., 2021), thus supporting its use for drug discovery studies. Significance was seen at the brain

region level across treatments (Onos et al., 2022), but pairwise interregional interactions were not

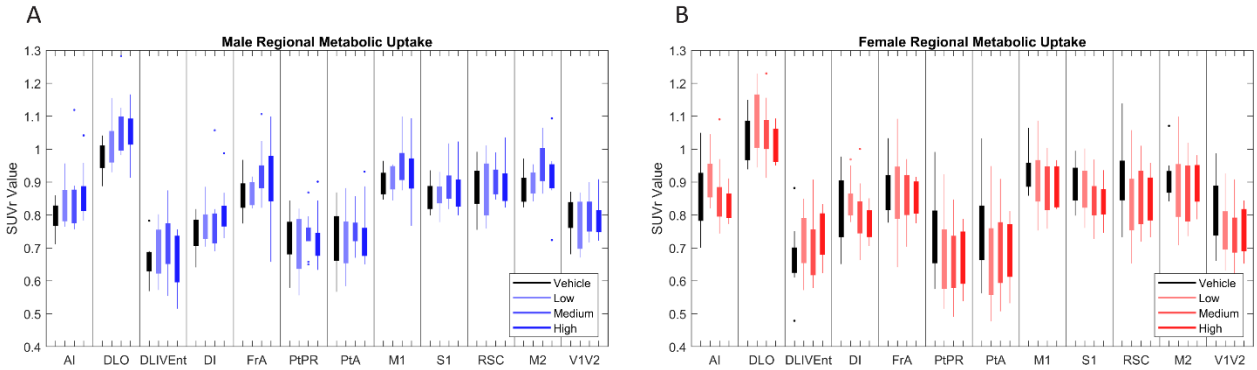


**Figure 2.** [18F]-FDG PET standardized uptake value ratio (SUVr) to cerebellum in brains regions in (A) male (N=39) and (B) female mice (N=38). Principle component analysis (PCA) found that the twelve brain regions above most consistently accounted for 80% of variance in cerebral metabolic uptake across cohorts. Full names of annotated brain region labels can be found in Supplementary Table 1.

explained by per-region significance, so a network approach (Jeub et al., 2018;Veronese et al., 2019;Chumin et al., 2023) was applied to further investigate interregional metabolic alterations.

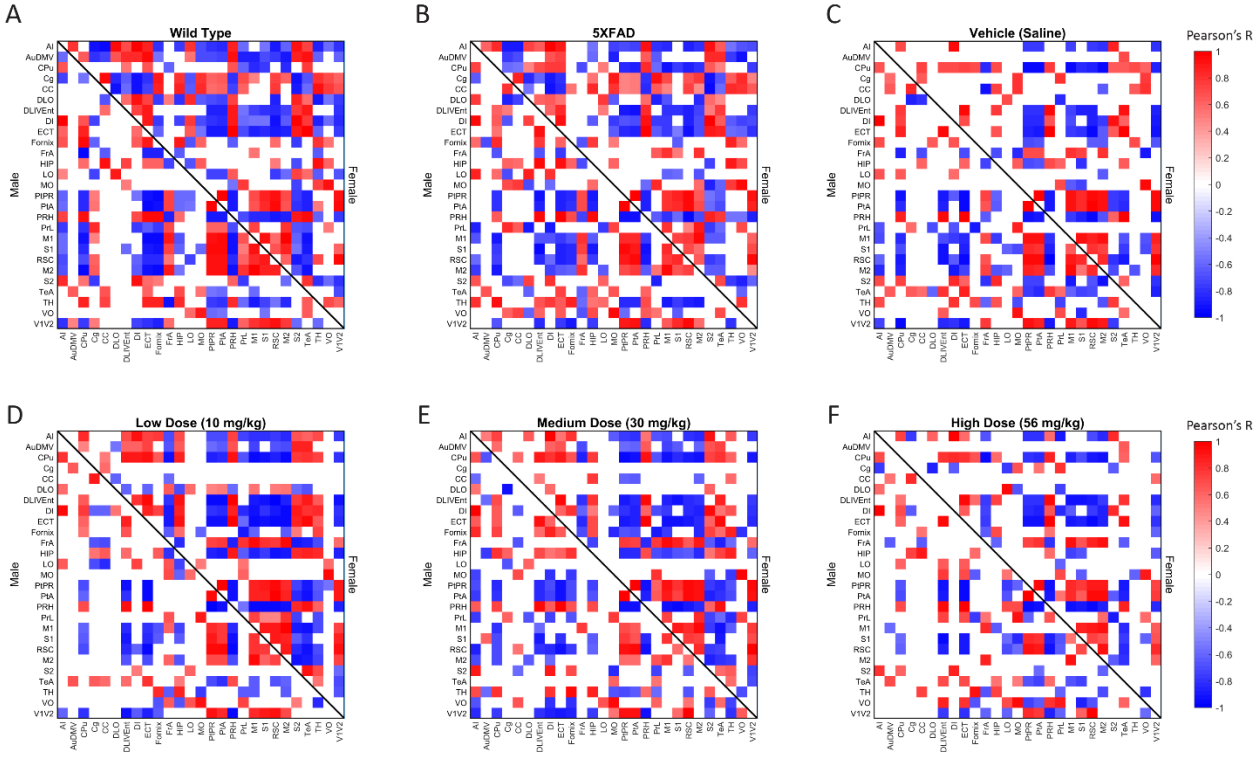


**Figure 3.** Thresholded metabolic covariance matrices sorted alphabetically by region. Edges were thresholded based on correlation magnitude, with surviving edges having a correlation significance value of $p<0.05$.

*Global Network Properties*

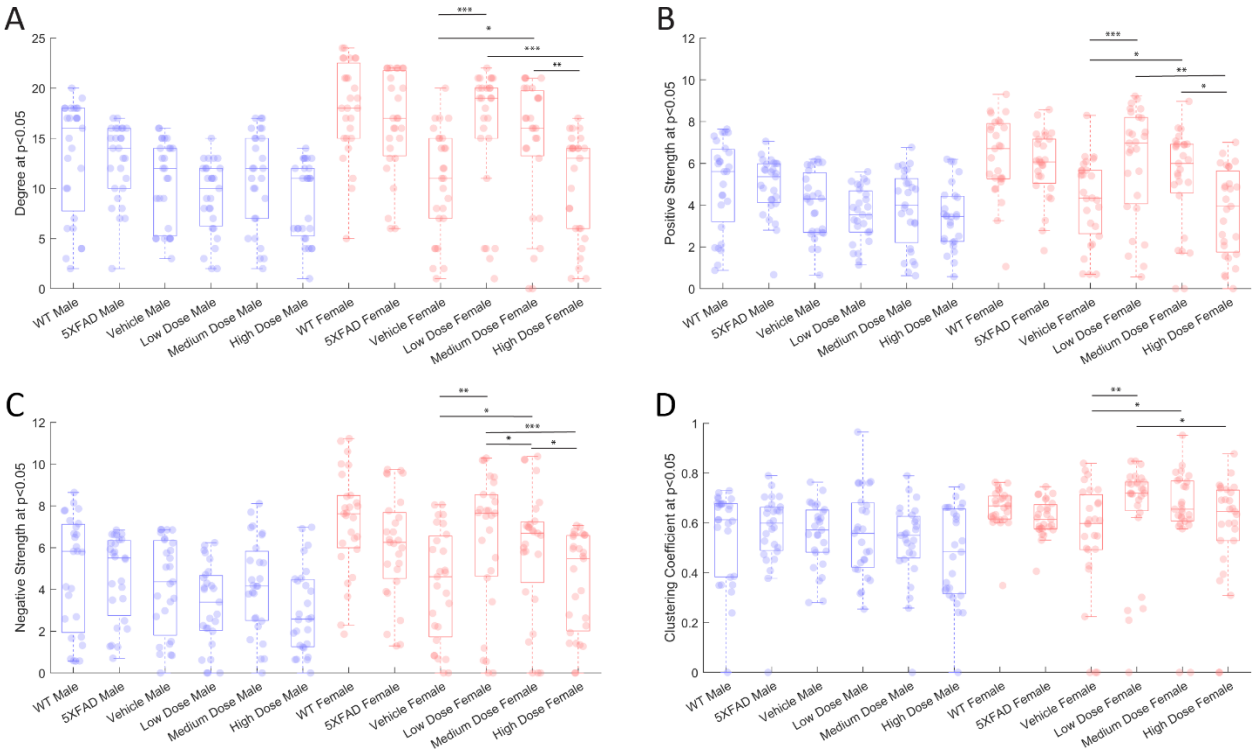


**Figure 4.** Properties of p<0.05 thresholded metabolic covariance for control and treatment groups. (A) Network degree, (B) positive strength, (C) negative strength, and (D) clustering coefficient. * denotes p < 0.05, ** denotes p<0.01, *** denotes p<0.005, 2-sample Kolmogorov-Smirnov test significance.

To measure metabolic changes at a network level, we utilized covariance and connectomic analyses (Jeub et al., 2018;Veronese et al., 2019;Chumin et al., 2023). First, we measured the degree of functional metabolic connectivity on a single-region basis, and extrapolated nodal degree values to a global distribution. For female mice, the network degree of vehicle dose and low dose ($p$<0.001), vehicle dose and medium dose ($p$<0.05), medium dose and high dose ($p$<0.01), and low dose and high dose ($p$<0.001) were significantly different. Interestingly, the vehicle dose and high dose had almost the same network distribution for degree ($p$=0.994), consistent with the findings of previous literature (Palop et al., 2007). By contrast, male mice did not follow the same degree changes observed in females, with no two distributions significantly different from one another between treatments (Figure 4A). Qualitatively, we see different connectivity patterns between sexes as a function of treatment. Males displayed oscillatory behavior in degree distributions, with the vehicle group more connected than low and high doses, but less connected than medium dose. By contrast, female mice showed a clear dose-dependent change in

degree of connections, with the networks of low and medium dosed mice significantly more connected

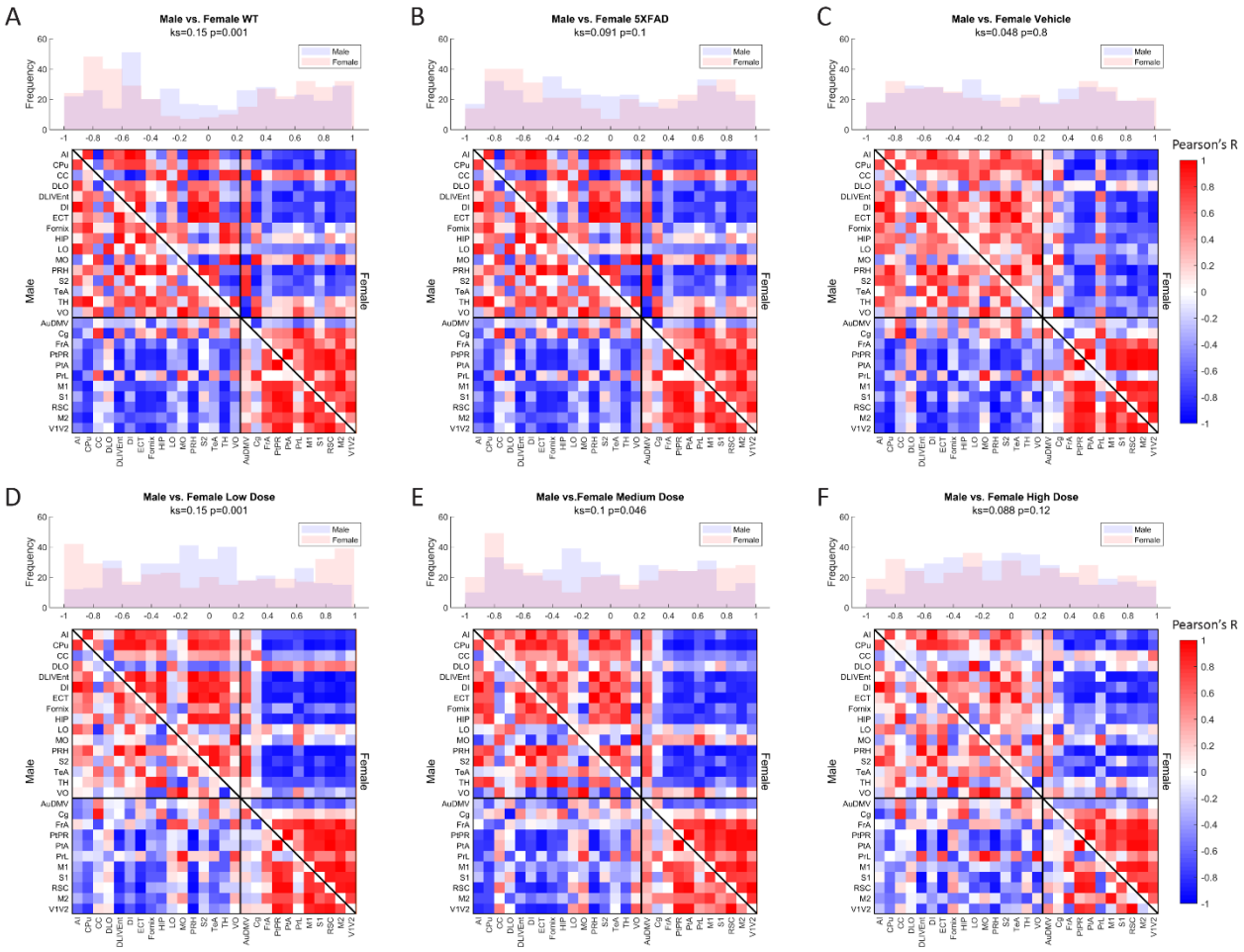


**Figure 5.** Metabolic ([18F]-FDG) covariance matrices for (A) wild-type (WT) (N=22, n=11 male, n=11 female), (B) 5XFAD (N=22, n=10 male, n=12 female), (C) saline vehicle dose (N=17, n=9 males, n=8 females), (D) low dose (N=21, n=10 males, n=11 females), (E) medium dose (N=20, n=10 males, n=10 females), and (F) high dose (N=19, n=10 males, n=9 females) treatment groups with male WT community partitions applied on upper (female) and lower (male) triangles. Histograms of interregional correlation values indicate correlation distribution across all brain regions for each respective cohort. Covariance was computed as Pearson's correlation of z-scored regional SUVR values across animals within each group. Distributions between sexes of a given cohort are compared with a 2-sample Kolmogorov-Smirnov (KS) nonparametric test, with KS-value and p-value printed above the histogram.

than those of the vehicle and high dosed mice. To look further into the weight and sign of functional connections between regions, we analyzed the positive and negative weighted node degree of every region in the brain, known and positive and negative strength, respectively. In females, the distributions of positive node strengths across the brain after a $p<0.05$ threshold was applied significantly differed between vehicle and low dose ($p<0.001$), vehicle and medium dose ($p<0.05$), medium and high dose ($p<0.01$), and low and high dose ($p<0.01$). Negative strengths in females resembled positive strengths in their distributions across treatment, both qualitatively in the same inverted paraboloid shape (see Figure

4B,C), and quantitatively with significant differences between the same groups as positive strengths, with the addition of significance between low and medium dose ($p<0.05$) not seen in positive strengths. Males did not show any significant differences between distributions of either positive or negative strengths after a $p<0.05$ threshold was applied to the covariance matrix. To measure the functional interconnectivity of brain subnetworks, clustering coefficients (propensity of connected triangles in a network) were calculated and compared in the same manner as the prior network characteristics. The clustering coefficients of brain networks followed a similar pattern across treatment for each sex. Significance was seen in the distribution of clustering coefficient in female networks between vehicle dose and low dose ($p<0.01$), vehicle dose and medium dose ($p<0.05$) and low dose and high dose ($p<0.05$), while males did not show significant differences that survived the $p<0.05$ threshold.

*Effect of Treatment on Covariance Distributions*

Distributions of Pearson's correlation between regions denoted by edge weight differed across sex and treatment, as measured by a two-sample KS non-parametric distribution comparison (see Figures 5-7). Males exhibited little handling stress, with qualitatively similar partitioned adjacency and edgewise distribution between 5XFAD disease control and saline-dosed vehicle cohorts (Figure 6B). Males treated chronically with a low dose (10 mg/kg) of LEV yielded a more normally distributed set of edgewise covariance trending towards significance compared to the vehicle (saline) treatment group of the same sex (KS = 0.01, $p = 0.057$). By contrast, males treated with the high dose (56 mg/kg) of LEV yielded a covariance distribution significantly different from the vehicle treated group (KS = 0.12, $p < 0.05$) (Figure 5E). Unlike males, females exhibited relationships in $^{18}$F-FDG covariance between treatments in the medium (30 mg/kg) and high (56 mg/kg) doses groups which trended towards significance (Figure 7D,E). Importantly, there was a significant sex effect with treatment distributions, where male and female cohorts were significantly different between low (KS = 0.15, $p < 0.005$) and medium (KS = 0.1, $p < 0.05$) dose, with males qualitatively more normally distributed than females (Figure 5).

*Community Structure and Component Function with Sex*

310 Metabolic covariance networks were assessed via the MRCC community detection algorithm with 10,000
311 permutations to establish a rigorous partition for covariance networks focused on positive covariance
312 between regions (Veronese et al., 2019;Chumin et al., 2023) where partitions, or communities, differed
313 between sexes and treatments. Female modularity ranged from two to five communities within a network,
314 with the number of partitions generally increasing linearly as a function of dose. Male modularity
315 consistently had more partitions relative to females, with the lowest number of modules present in the
316 low dose group and an average of 5.66 modules across other treatments. We interpreted the number of
317 communities as indicative of edgewise coherence among regions, akin to functional subnetworks. We
318 observe that males generally exhibit a greater number of subnetworks relative to females. This agrees
319 with our findings from the observations of node degree and strength distributions. Males form
320 subnetworks of highly similar metabolic covariance, while the most similar partition structure for females
321 tends towards large, bidirectional networks, consistent with higher degrees of connectivity across regions
322 relative to males across treatments groups. To track network changes in a common reference space, we
323 imposed the community structure of the healthy control WT male metabolic covariance network onto
324 male and female network of the same treatment across all treatments (Figure 5). Male littermate controls
325 were chosen as the reference network partition due to consensus findings of females displaying more
326 aggressive AD disease phenotype at a given age, both in the 5XFAD model and in human AD pathology
327 (Oblak et al., 2021). Using male littermate controls therefore enabled better tracking of deviations from a

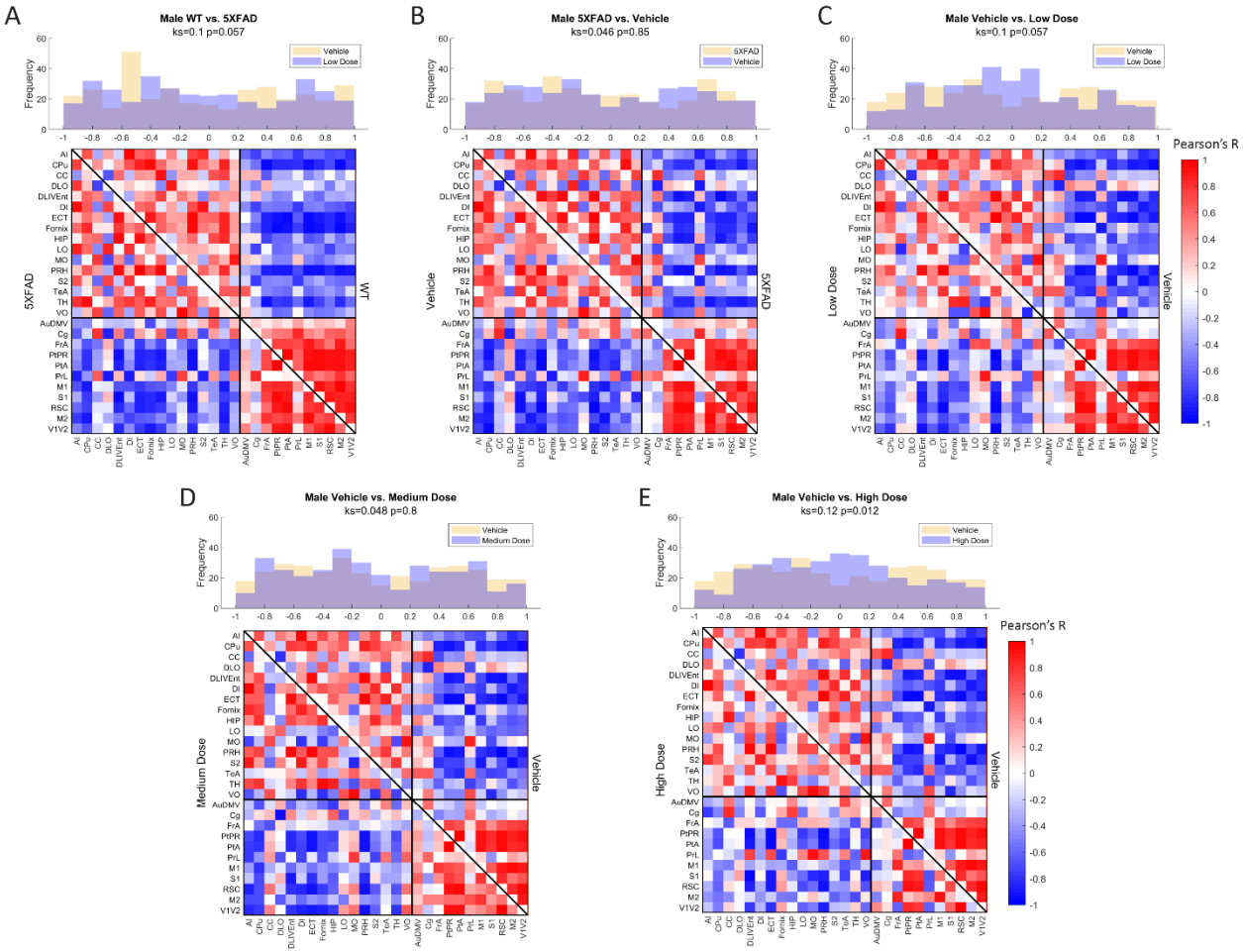


**Figure 6.** Male metabolic covariance matrices across treatment with WT community partitions applied. Changes in functional network structure can be observed via (A) changes in network and covariance distribution due to disease (N=21, n=11 WT, n=10 5XFAD), (B) handling stress (N=19, n=10 5XFAD, n=9 vehicle), (C) low (N=19, n=9 vehicle, n=10 low dose), (D) medium (N=19, n=9 vehicle, n=10 medium dose), and (E) high (N=19, n=9 vehicle, n=10 high dose) dose difference.

healthy metabolic network. To assess differences in metabolic uptake distributions in subnetworks between males and females at a given treatment, we performed ANOVA between male and female metabolic SUVr networks clustered by WT male MRCC partitions. Significance was corrected for multiple comparisons via Bonferroni correction. We found that at vehicle, low, and high dose, there were no significant differences in metabolic uptake in communities of the same regional groupings between sexes; however, at low dose, of the two communities detected in the male MRCC algorithm, one yielded significantly different metabolic uptake. The first community was composed of the following region members: AI, CPu, CC, DLO, DLIVEnt, DI, ECT, Fornix, HIP, LO, MO, PRH, S2, TeA, TH, and VO (See Supplemental Table 1 for full region names). At low dose, females exhibited significantly more uptake in

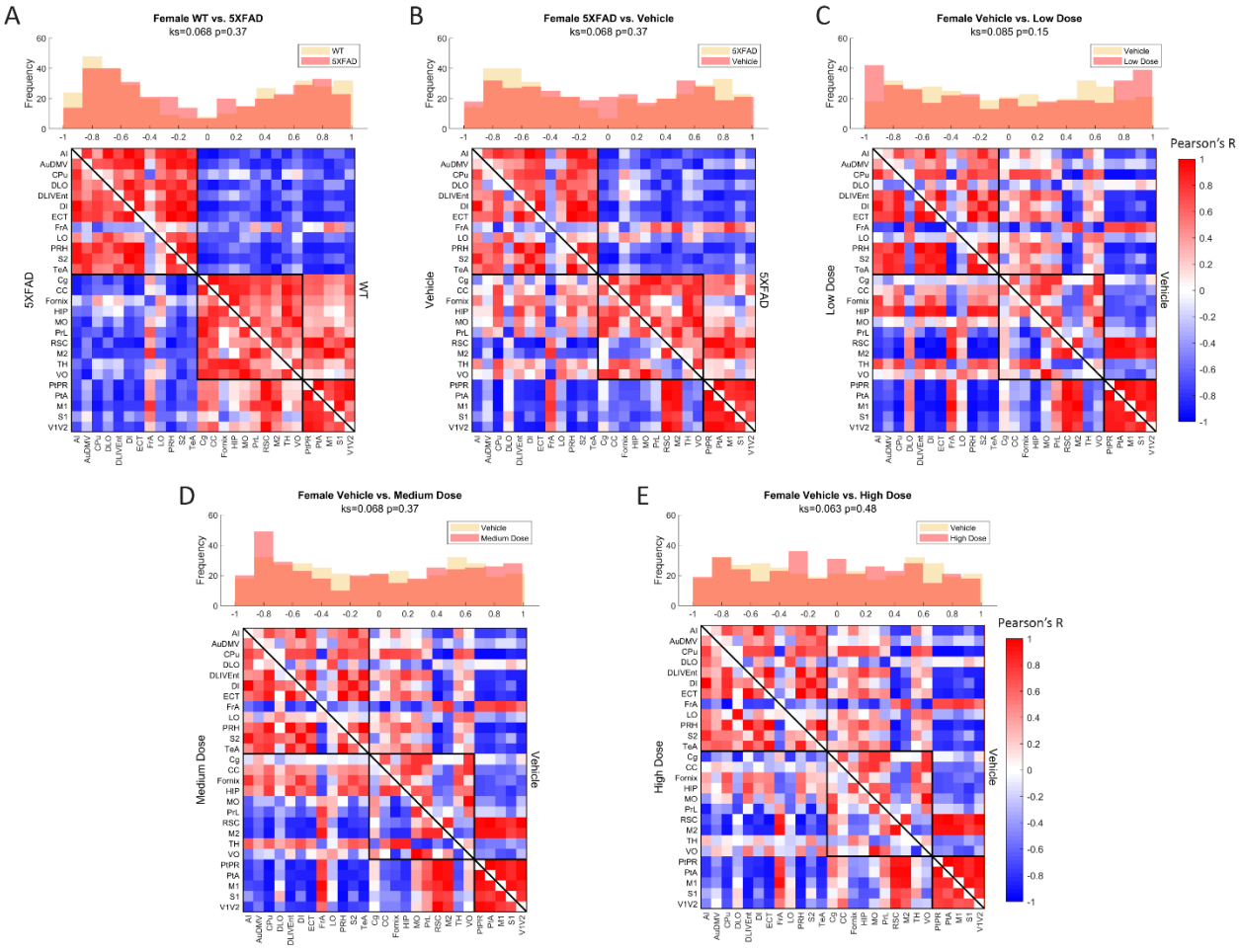


**Figure 7.** Female metabolic covariance matrices across treatment with WT community partitions applied. Changes in functional network structure can be observed via (A) changes in network and covariance distribution due to disease (N=23, n=11 WT, n=12 5XFAD), (B) handling stress (N=20, n=12 5XFAD, n=8 vehicle), (C) low (N=19, n=8 vehicle, n=11 low dose), (D) medium (N=18, n=8 vehicle, n=10 medium dose), and (E) high (N=17, n=8 vehicle, n=9 high dose) dose difference.

this subnetwork than males (F = 4.9, $p<0.05$). The functional interpretation of this subnetwork, using equally weighted components, was determined to be primarily learning, with additional components of perception and sensory processing. Within sex, males displayed significantly different metabolic uptake between vehicle and medium dose in the subnetwork containing AuDMV, Cg, FrA, PtPR, PtA, PrL, M1, S1, RSC, M2, and V1V2 (F = 4.7, $p<0.05$). Functionally, the regions within this subnetwork encoded primarily for learning and sensory processing. Females did not display significantly different uptake in common communities between treatments.

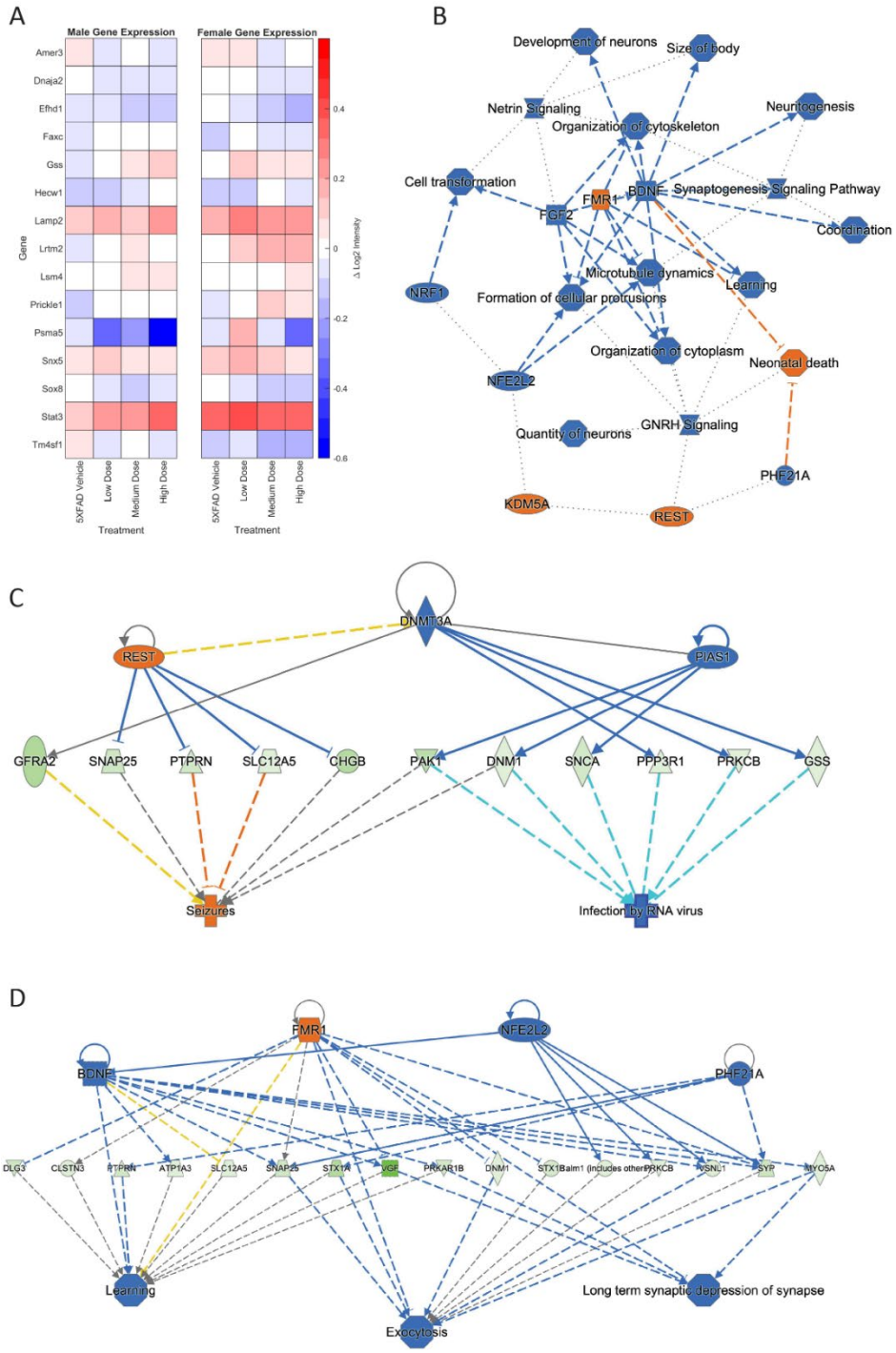


**Figure 8.** Hemisagittal mouse brain sections were homogenized and analyzed through nanoString. (A) Log2 intensity gene expression in male (n=39) and female (n=38) 5XFAD treatment groups from male and female WT vehicle groups, respectively. Gene expression at treatment level was subtracted from expression at vehicle, and results plotted as a heat map. Genes plotted are linked to AD, epileptiform activity, cerebral metabolism, and/or cerebral homeostatic mechanisms. (B) Primary GO pathway analysis found the processes connected to similarly expressed genes between medium and high dosed female mice. Further pathway analysis focused found connections to (C) seizure, (D) learning, exocytosis, and long-term depression functions. See Supplementary figure 1 for prediction legend.

347 Brain hemispheres were assessed via nanoString for gene expression differences using a panel
348 based on human AD gene expression changes (Allen et al., 2016;Mostafavi et al., 2018;Wang et al.,
349 2018;Preuss et al., 2020;Wan et al., 2020). Linear regression analysis revealed 15 genes that were
350 significant at $p<0.05$ for genotype, sex, and/or treatment. As shown in Figure 8A, the change in log2
351 intensities from WT vehicle mice demonstrated undirected significant dose-specific effects for genes
352 which encode for AD, epileptiform activity, cerebral metabolism, and/or cerebral homeostatic
353 mechanisms. Further analyses were performed on genes from medium and high dose treated animals
354 that were significantly anti-correlated with neuronal-related human modules in the inferior frontal gyrus
355 (IFG) region (Wan et al., 2020). This gene module identified 129 genes, and Gene ontology (GO)
356 enrichment analysis identified a number of biological processes, which, consistent with the mechanism
357 of action of LEV (Dubovsky et al., 2015), included synaptic vesicle cycling, vesicle exocytosis, vesicle
358 recycling, vesicle priming, regulated exocytosis, neurotransmitter transport, neurotransmitter secretion,
359 and protein localization to cellular junctions (Wan et al., 2020;Onos et al., 2022) (see Figure 8B). Further
360 pathway analyses performed on these 129 genes with Ingenuity Pathway Analysis (IPA) (Kramer et al.,
361 2014) revealed significant overlap with canonical pathways 'SNARE signaling pathway', 'Netrin
362 Signaling', 'Synaptogenesis signaling pathway', 'mitochondrial dysfunction' and 'Glutaminergic Receptor
363 Signaling pathway (enhanced)'. Top regulator effect networks were also identified, such as' 'Exocytosis
364 and Learning' comprised of *BDNF*, *FMR1*, *NFE2L2* and *PHF21A*, and 'Seizures' comprised of *DNMT3A*,
365 *PIAS1* and *REST*. Lastly, 'memantine' was determined to be both a significant upstream regulator and
366 driver of the causal network. Memantine (Lipton, 2006), also known as Namenda, was one of the first
367 approved drugs to treat AD and has a similar target to LEV: it works as an NMDA receptor antagonist
368 aimed at quelling abnormal activity in the brain. Overall, identification of specific processes and pathways
369 relevant to drug treatment help to narrow mechanisms and refine preclinical translation from mouse to
370 human studies.
371

372 *Exposure-Response Modeling*

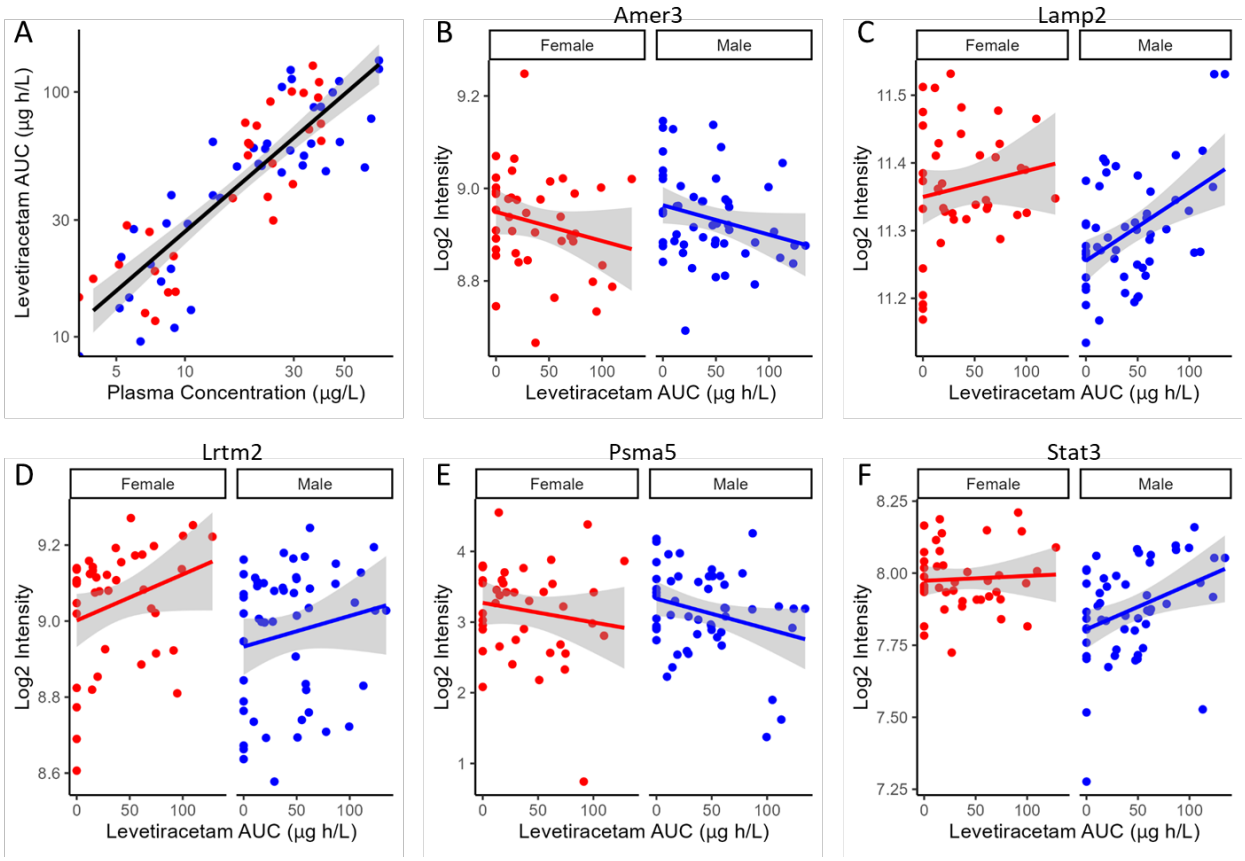


**Figure 9.** PK/PD plots of Log2 Intensity as a function of levetiracetam exposure for (A) Amer3, (B) Lamp2, (C) Lrtm2, (D) Psma5, and (E) Stat3 expression are associated with predicted levetiracetam exposure (AUC) using a linear PK/PD model. Solid red (female) and blue (male) lines indicate linear regression, while shaded region represent the 95% confidence interval.

| | AUC β± SE (p-value) | Sex β± SE (p-value) | $R^2$ |
|---|---|---|---|
| Amer3 | -0.006 ± 0.0003 (0.024) | 0.014 ± 0.021 (0.5) | 0.04 |
| Lamp2 | 0.00075 ± 0.0002 (0.0013) | -0.069 ± 0.017 (<0.001) | 0.21 |
| Lrtm2 | 0.00098 ± 0.00046 (0.04) | -0.085 ± 0.035 (0.02) | 0.078 |
| Psma5 | -0.0036 ± 0.0017 (0.04) | -0.0016 ± 0.13 (0.99) | 0.025 |
| Stat3 | 0.001 ± 0.0004 (0.16) | -0.11±0.03 (<0.001) | 0.16 |

**Table 1.** Association between gene expression and levetiracetam exposure area under the curve (AUC) and sex. Modelling was calculated in R using lm(Y~AUC+SEX).

373 Despite the plasma concentration AUC relationship and the dose dependent changes observed with
374 metabolic connectomics, no apparent relationships could be established with connectomics data when
375 PK/PD modelled using a multi-linear regression. By contrast, expression changes in Amer3, Lamp2,
376 Lrtm2, Psma5, and Stat3 all showed significant associations ($p$<0.05) with LEV concentration and/or
377 animal sex (Table 1, Figure 9).

378

379 **DISCUSSION**

380 In the current study, we performed retrospective network analysis of LEV data to gain novel insight
381 about how chronic dosing affects AD progression as it pertains to cerebral metabolic uptake and gene
382 expression. Our results show that 6-month-old 5XFAD mice display significant changes in metabolic
383 uptake as seen by network analyses correlated within and between regions in both sexes and across
384 treatment. Per previous studies, we conducted general linear statistical modeling of regional $^{18}$F-FDG
385 uptake data as a measure of regional brain function. Quantitative analysis of these data revealed a sex-
386 by-dose relationship (Onos et al., 2022); however, due to limitations of these approaches, post-hoc
387 analysis only permitted pair-wise analysis of regional data, thus negating the inter-regional network
388 changes that support higher brain function (Chumin et al., 2023). To overcome this, we applied network
389 covariance analysis to $^{18}$F-FDG data, which has been shown to distinguish stage of disease for both
390 preclinical (Chumin et al., 2023) and clinical AD (Veronese et al., 2019). Using this approach, we
391 quantified pairwise network covariance for all regions, then computed edgewise network features by
392 calculating distributions of degree, positive and negative strength, and clustering coefficient in metabolic
393 networks from thresholded networks. We extrapolated per-region node characteristics to global
394 distributions and compared changes in distributions between treatment within sex. At 6 months, female
395 mice displayed significantly more interregional metabolic uptake as seen by the degree and density of
396 both diseased mice and their littermate controls (Figure 4). Overall, network characteristics indicated that
397 the magnitude of interregional metabolic correlation decreased as chronic dose concentration increased
398 in males, as seen in global degree, and strength outputs. In females, disease and handling stress
399 decreased interregional functional connectivity, some of which was recovered in a dose-dependent
400 manner. Females dosed chronically at 10 mg/kg showed the greatest metabolic network change across
401 analyses, consistent with the mode of action of LEV. More generally, network alteration was inversely
402 proportional to dose concentration in females (Figure 4).

403 Differences in uptake in control cohorts were not localized to specific communities between sexes
404 in 5XFAD mice when the male community partition was applied to both groups, but differences were
405 localized to module 1 of the male partition structure in WT mice ($p$<0.05, Bonferroni corrected). While

406 vehicle, medium, and high doses did not exhibit significantly different uptake between like communities,
407 low dose male and female mice exhibited significant differences in metabolic uptake in one of two
408 modules. Based on the region members of this module, these changes are expected to impact learning,
409 memory, and sensory integration, and are consistent with LEV mode of action.

410 5XFAD is known to be an aggressive amyloidogenic early-onset model of Alzheimer's disease.
411 Like AD, 5XFAD mice exhibit sexual dimorphism in pathology, with females displaying a more rapid onset
412 disease phenotype (Oblak et al., 2021). Previous studies have presented conflicting findings on cerebral
413 metabolic uptake in the 5XFAD model around 6 months (Oblak et al., 2021). In the current study, we treat
414 littermate controls as a reference population and explore the changes of metabolic networks with respect
415 to littermate controls. We hypothesized that within sex, we would see a dose-dependent response evident
416 in network characteristics and community structure. We also hypothesized that this dose-dependency
417 would vary between sexes, with females showing a greater restorative response in part due to their faster
418 progression towards disease state.

419 Comparing littermate controls to diseased (5XFAD) mice, there were surprisingly few differences
420 in male and female adjacency matrices when community partition structure of their WT littermates was
421 applied. By contrast, female 5XFAD mice exhibited a greater handling stress response than males, and
422 this stress response was localized to interregional correlation shifts in the retrosplinial cortex (RSC) and
423 secondary motor cortex (M2). This is consistent with amyloid deposition previously reported for these
424 structures (Oblak et al., 2021). This handling effect was observed in all female LEV dosed cohorts (see
425 Figure 7B-E). At low dose, neither females nor males had network alterations significantly different from
426 vehicle, though males trended towards significance. At medium dose, females showed qualitative
427 differences in network structure compared to vehicle in the interregional correlations of the frontal
428 association cortex as well as the lateral orbitofrontal cortex. Males showed similar qualitative differences
429 in lateral orbitofrontal correlations, but neither sex differed from vehicle at the medium dose. At high dose,
430 males significantly differed from vehicle in edgewise correlations with many weak correlations relative to
431 vehicle ($p<0.05$) (Figure 6E). Females, on the other hand, did not display significant edgewise
432 distributions, and instead converged back towards vehicle distribution relative to medium and low dose.

433 This finding is consistent with dose-dependent findings of previous LEV studies (Onos et al., 2022); at
434 high chronic doses of LEV, females both in mice as well as in the clinic develop a functional resistance
435 to the drug, the exact cause of which is yet to be uncovered (Löscher and Schmidt, 2006;Surges et al.,
436 2008;Sanchez et al., 2012;Onos et al., 2022).WT covariance distributions were significantly different
437 between males and females ($p$<0.005). Females display a greater number of strong correlations, both
438 positive and negative, between regions. This is consistent with previous literature showing that WT
439 females show marginally greater glycolytic metabolism in the brain after ~6 months of age (Oblak et al.,
440 2021). 5XFAD mice displayed no significant difference in their distributions, however, females did show
441 a bimodal distribution with the highest frequency of covariance values occurring at the limits. In low and
442 medium doses, female edgewise distributions were again bimodal and significantly different from males
443 ($p$<0.005 and $p$<0.05, respectively). These differences further reinforce the sexual dimorphism of 5XFAD
444 mice which has been previously reported (Oblak et al., 2021;Onos et al., 2022;Chumin et al.,
445 2023;Jullienne et al., 2023), and are thought to be linked to the transgene expression being linked to the
446 estrogen sensitive Thy1 promoter (Moechars et al., 1996).

447 Network analyses of thresholded metabolic correlation networks, like edgewise distributions,
448 revealed network characteristics that differed on a sex by treatment basis. WT mice follow a pattern with
449 females' retaining greater numbers of nodes than their male counterpart, as seen in network degree and
450 clustering coefficient distributions (Figure 3A,D). Vehicle cohorts showed a sex-specific decrease in
451 density relative to WT and likely represents handling stress. This handling stress is consistent with prior
452 findings which show that female mice exhibit higher stress hormone response than their male
453 counterparts when introduced to handling stressors (Sensini et al., 2020). At low and medium dose, we
454 see network degree approach WT levels only to decline at a high dose of LEV, which we interpreted as
455 due to functional tolerance. Further analysis of positive and negative network strengths support the sex
456 and dose dependency in whole brain networks. Females contain more positive and negative strengths
457 than males at every treatment, and the low and medium LEV doses show a significant increase in positive
458 and negative strengths (Figure 4B,C). This supports the notion that in AD pathology, signal disruption is
459 seen both in suppression of some circuits and aberrant activity of others, resulting in more extreme

460 interregional relationships (Palop et al., 2007). Previous studies (Palop, 2009;Sanchez et al., 2012;Onos
461 et al., 2022) have reported that LEV reduces sub-seizure epileptiform activity in mouse models of AD
462 (Chumin et al., 2023) and we believe that by reducing aberrant neuronal activity, LEV perturbs
463 hyperactive neural circuitry back towards a functional equilibrium with decreased signal suppression
464 distal to Aβ plaques and a regulation of aberrant activity near plaques. However, specificity between
465 equilibrium metabolic uptake in neurons, glia, and other energy-demanding cerebral machinery and
466 nonequilibrium inflammation-driven metabolic uptake in microglia and hyperactive dysregulated circuits
467 cannot be distinguished in $^{18}$F-FDG PET imaging (Xiang et al., 2021). Because we were unable to
468 empirically differentiate between cerebral metabolic contributors due to the retrospective nature of the
469 current study, we conducted targeted transcriptomic analysis using nanoString to track gene expression
470 and identified fifteen genes to be dose and sex dependent (See Figure 8A). Further analyses examining
471 GO biological processes and pathway overlap in genes shared between medium and high-dosed animals
472 were primarily representative of synaptic function and organization as it pertains to neural activity. REST
473 gene activation, whose pathway causes suppression of genes related to epileptiform activity and seizures
474 was identified as a pathway, as was the FMR1 pathway, implicated in the activation of genes associated
475 with synaptic depression and learning (see Figure 8C and D, respectively), which is consistent with LEV's
476 mode of action. Together, these pathways contribute to a larger transcriptional network at play in mice
477 treated with LEV composed primarily of neuronal maintenance and restoration (Figure 8B). This was not
478 overly surprising, as the genes analyzed were selected as they were correlated with human AD genes in
479 the Neuronal Consensus cluster. However, connecting gene pathways to metabolic uptake helped to link
480 cerebral metabolic allocation corresponding to LEV treatment in a way that is currently unattainable by
481 PET alone.

482 As with all studies, there are limitations that must be considered when drawing conclusions. First,
483 the 5XFAD model was developed as a rapid-onset, highly aggressive representation of early-onset
484 Alzheimer's disease. 5XFAD displays early amyloid beta plaque formation relative to other mouse models
485 and epileptiform activity localized to the dentate gyrus and hippocampus, spatially analogous to human
486 data (Abe et al., 2020). However, 5XFAD mice have been shown not to express behavioral disease

487 phenotype relative to controls analogous to MCI and AD patients in the clinic (Oblak et al., 2021). With
488 this in mind, the current study revealed novel interactions that can provide insight into cerebral metabolic
489 modulation by LEV in AD. LEV clearly acts in a dose and sex-dependent manner, with network alteration
490 relying on the degree of disease phenotype present in the subject. To more completely understand the
491 network effects of LEV, future studies might use less severe, more physiologically analogous mouse
492 models of AD, and bear in mind sexual dimorphism to test LEV efficacy in both sexes at equivalent
493 disease phenotypes. MODEL-AD is currently longitudinally testing novel models of AD, which may fulfill
494 these requirements (Oblak et al., 2020)] and studying the effect of LEV on disease progression in these
495 models may be more translationally viable. An additional limitation discussed in the original study is the
496 choice of LEV dose chronically administered to these mice (Onos et al., 2022). Future studies looking at
497 LEV's metabolic modulatory effects may choose more intermediate doses than the ones in this study
498 gain a more in-depth understanding of edgewise changes in community structures as well as between
499 regions. Analytical tools to connect regional components of functional metabolic correlation communities
500 to their emergent functional properties such as sensory, motor, or integration hubs are currently in
501 development, and will shed light on the nature of metabolic restructuring in terms of edgewise correlation
502 shifts.

503 Previous studies show that LEV likely acts near circuits or networks plagued by beta amyloid
504 deposition and that behavioral alterations can be tracked in a dose-dependent manner (Busche et al.,
505 2008;Sanchez et al., 2012). In the original PTC study, mice underwent $^{18}$F-AV45 PET imaging according
506 to the same protocols of the $^{18}$F-FDG imaging as well as behavioral evaluation (Onos et al., 2022). A lack
507 of significant change in behavioral and amyloid load differences led us to exclude these data in our
508 retrospective analysis. However, future studies utilizing PET imaging of amyloid deposition in mouse
509 models to map the co-localization of this structural network with the functional networks given by
510 metabolic PET imaging may shed more insight into metabolic perturbation of AD pathology with respect
511 to amyloid imaging. Moreover, combining these with transcriptomics and PK/PD modeling could lead to
512 a more precise indication of drug efficacy. This, in turn, would have significant translational implications

513 for precision medicine and treatment of the synchronized hyperactive neural activity seen in patients with
514 AD.

515 In the previous study, gene expression analysis revealed that in an Accelerating Medicines
516 Partnership Program for Alzheimer's Disease (AMP AD) consensus clusters of genes, females exhibit
517 anticorrelation in gene expression with respect to analogous human expression, suggesting that at high
518 chronic dosing of LEV, there may be effects seen that cannot be explained by our functional tolerance
519 interpretation (Preuss et al., 2020;Onos et al., 2022). Future work may utilize a multimodal approach
520 involving higher throughput and/or spatial transcriptomics coupled with metabolic uptake quantification
521 to better resolve ambiguities in the physiological effects of LEV dose-wise.

522 In conclusion, our research revealed significant dose-dependent changes in region-wise glycolytic
523 correlation and gene expression changes in response to LEV not possible with traditional general linear
524 statistical modeling. Further, it revealed a sex and dose dependency that provides a means to track
525 network changes using translationally relevant $^{18}$F-FDG PET imaging.

526

527 **Data Availability:** All protocols, raw, and summary data are available at https://adknowledgeportal.org,
528 where the Synapse ID is syn2580853, and DOI is 10.7303/syn2580853.

529

530 **Acknowledgements:** The authors would like to acknowledge the JAX Center for Biometric Analysis staff
531 for support of the chronic dosing studies. In addition, we would like to acknowledge the JAX Genome
532 Technologies core for assistance with nanoString RNA extractions and sample processing. The current
533 study data, in whole or in part, were obtained from the AD Knowledge Portal
534 (https://adknowledgeportal.org), and the brain covariance analysis software was obtained from the
535 publicly available CovNet package (https://github.com/echumin/CovNet).

536

537 **Competing Interests:** The authors do not report any competing interests.

538

539 **Funding Sources:** The data for this study were funded through grant NIA U54AG054345.

540 **References**

541 Abe, Y., Ikegawa, N., Yoshida, K., Muramatsu, K., Hattori, S., Kawai, K., Murakami, M., Tanaka,
542 T., Goda, W., Goto, M., Yamamoto, T., Hashimoto, T., Yamada, K., Shibata, T., Misawa,
543 H., Mimura, M., Tanaka, K.F., Miyakawa, T., Iwatsubo, T., Hata, J.-I., Niikura, T., and
544 Yasui, M. (2020). Behavioral and electrophysiological evidence for a neuroprotective role
545 of aquaporin-4 in the 5xFAD transgenic mice model. *Acta Neuropathologica*
546 *Communications* 8.

547 Allen, M., Carrasquillo, M.M., Funk, C., Heavner, B.D., Zou, F., Younkin, C.S., Burgess, J.D.,
548 Chai, H.S., Crook, J., Eddy, J.A., Li, H., Logsdon, B., Peters, M.A., Dang, K.K., Wang, X.,
549 Serie, D., Wang, C., Nguyen, T., Lincoln, S., Malphrus, K., Bisceglio, G., Li, M., Golde,
550 T.E., Mangravite, L.M., Asmann, Y., Price, N.D., Petersen, R.C., Graff-Radford, N.R.,
551 Dickson, D.W., Younkin, S.G., and Ertekin-Taner, N. (2016). Human whole genome
552 genotype and transcriptome data for Alzheimer's and other neurodegenerative diseases.
553 *Sci Data* 3**,** 160089.

554 Angulo, S.L., Henzi, T., Neymotin, S.A., Suarez, M.D., Lytton, W.W., Schwaller, B., and Moreno,
555 H. (2020). Amyloid pathology-produced unexpected modifications of calcium
556 homeostasis in hippocampal subicular dendrites. *Alzheimer's & Dementia* 16**,** 251-
557 261.

558 Bakker, A., Albert, M.S., Krauss, G., Speck, C.L., and Gallagher, M. (2015). Response of the
559 medial temporal lobe network in amnestic mild cognitive impairment to therapeutic
560 intervention assessed by fMRI and memory task performance. *Neuroimage-Clinical* 7**,**
561 688-698.

562 Bakker, A., Gregory, Marilyn, Caroline, Lauren, Craig, Michael, Susan, Amy, and Gallagher, M.
563 (2012). Reduction of Hippocampal Hyperactivity Improves Cognition in Amnestic Mild
564 Cognitive Impairment. *Neuron* 74**,** 467-474.

565 Busche, M.A., Eichhoff, G., Adelsberger, H., Abramowski, D., Wiederhold, K.H., Haass, C.,
566 Staufenbiel, M., Konnerth, A., and Garaschuk, O. (2008). Clusters of hyperactive neurons
567 near amyloid plaques in a mouse model of Alzheimer's disease. *Science* 321**,** 1686-1689.
568 Chumin, E., Burton, C., Silvola, R., Miner, E., Persohn, S., Veronese, M., and Territo, P. (2023).
569 Brain Metabolic Network Covariance and Aging in a Mouse Model of Alzheimer's
570 Disease. *bioRxiv***,** 2023.2006.2021.545918.
571 Dubovsky, S.L., Daurignac, E., Leonard, K.E., and Serotte, J.C. (2015). Levetiracetam, Calcium
572 Antagonism, and Bipolar Disorder. *J Clin Psychopharmacol* 35**,** 422-427.
573 García-Pérez, E., Mahfooz, K., Covita, J., Zandueta, A., and Wesseling, J.F. (2015).
574 Levetiracetam accelerates the onset of supply rate depression in synaptic vesicle
575 trafficking. *Epilepsia* 56**,** 535-545.
576 Jeub, L.G.S., Sporns, O., and Fortunato, S. (2018). Multiresolution Consensus Clustering in
577 Networks. *Scientific Reports* 8.
578 Jullienne, A., Szu, J.I., Quan, R., Trinh, M.V., Norouzi, T., Noarbe, B.P., Bedwell, A.A., Eldridge,
579 K., Persohn, S.C., Territo, P.R., and Obenaus, A. (2023). Cortical cerebrovascular and
580 metabolic perturbations in the 5xFAD mouse model of Alzheimer's disease. *Front Aging*
581 *Neurosci* 15**,** 1220036.
582 Klee, J.L., Kiliaan, A.J., Lipponen, A., and Battaglia, F.P. (2020). Reduced firing rates of
583 pyramidal cells in the frontal cortex of APP/PS1 can be restored by acute treatment with
584 levetiracetam. *Neurobiology of Aging* 96**,** 79-86.
585 Kramer, A., Green, J., Pollard, J., Jr., and Tugendreich, S. (2014). Causal analysis approaches
586 in Ingenuity Pathway Analysis. *Bioinformatics* 30**,** 523-530.
587 Kumar, A., Maini, K., and Kadian, R. (2023). "Levetiracetam," in *StatPearls*. (Treasure Island
588 (FL)).

589 Lippa, C.F., Rosso, A., Hepler, M., Jenssen, S., Pillai, J., and Irwin, D. (2010). Levetiracetam: a
590 practical option for seizure management in elderly patients with cognitive impairment. *Am*
591 *J Alzheimers Dis Other Demen* 25**,** 149-154.
592 Lipton, S.A. (2006). Paradigm shift in neuroprotection by NMDA receptor blockade: memantine
593 and beyond. *Nat Rev Drug Discov* 5**,** 160-170.
594 Löscher, W., and Schmidt, D. (2006). Experimental and Clinical Evidence for Loss of Effect
595 (Tolerance) during Prolonged Treatment with Antiepileptic Drugs. *Epilepsia* 47**,** 1253-
596 1284.
597 Lynch, B.A., Lambeng, N., Nocka, K., Kensel-Hammes, P., Bajjalieh, S.M., Matagne, A., and
598 Fuks, B. (2004). The synaptic vesicle protein SV2A is the binding site for the antiepileptic
599 drug levetiracetam. *Proceedings of the National Academy of Sciences* 101**,** 9861-9866.
600 Magalhães, J.C., Gongora, M., Vicente, R., Bittencourt, J., Tanaka, G., Velasques, B., Teixeira,
601 S., Morato, G., Basile, L.F., Arias-Carrión, O., Pompeu, F.a.M.S., Cagy, M., and Ribeiro,
602 P. (2015). The Influence of Levetiracetam in Cognitive Performance in Healthy
603 Individuals: Neuropsychological, Behavioral and Electrophysiological Approach. *Clinical*
604 *Psychopharmacology and Neuroscience* 13**,** 83-93.
605 Minkeviciene, R., Rheims, S., Dobszay, M.B., Zilberter, M., Hartikainen, J., Fülöp, L., Penke, B.,
606 Zilberter, Y., Harkany, T., Pitkänen, A., and Tanila, H. (2009). Amyloid β-Induced
607 Neuronal Hyperexcitability Triggers Progressive Epilepsy. *The Journal of Neuroscience*
608 29**,** 3453-3462.
609 Moechars, D., Lorent, K., De Strooper, B., Dewachter, I., and Van Leuven, F. (1996). Expression
610 in brain of amyloid precursor protein mutated in the alpha-secretase site causes disturbed
611 behavior, neuronal degeneration and premature death in transgenic mice. *EMBO J* 15**,**
612 1265-1274.

613 Mostafavi, S., Gaiteri, C., Sullivan, S.E., White, C.C., Tasaki, S., Xu, J., Taga, M., Klein, H.U.,
614 Patrick, E., Komashko, V., Mccabe, C., Smith, R., Bradshaw, E.M., Root, D.E., Regev,
615 A., Yu, L., Chibnik, L.B., Schneider, J.A., Young-Pearse, T.L., Bennett, D.A., and De
616 Jager, P.L. (2018). A molecular network of the aging human brain provides insights into
617 the pathology and cognitive decline of Alzheimer's disease. *Nat Neurosci* 21**,** 811-819.
618 Musaeus, C.S., Shafi, M.M., Santarnecchi, E., Herman, S.T., and Press, D.Z. (2017).
619 Levetiracetam Alters Oscillatory Connectivity in Alzheimer's Disease. *Journal of*
620 *Alzheimers Disease* 58**,** 1065-1076.
621 Oblak, A.L., Forner, S., Territo, P.R., Sasner, M., Carter, G.W., Howell, G.R., Sukoff-Rizzo, S.J.,
622 Logsdon, B.A., Mangravite, L.M., Mortazavi, A., Baglietto-Vargas, D., Green, K.N.,
623 Macgregor, G.R., Wood, M.A., Tenner, A.J., Laferla, F.M., Lamb, B.T., And The, M.-A.,
624 and Consortium (2020). Model organism development and evaluation for late-onset
625 Alzheimer's disease: MODEL-AD. *Alzheimers Dement (N Y)* 6**,** e12110.
626 Oblak, A.L., Lin, P.B., Kotredes, K.P., Pandey, R.S., Garceau, D., Williams, H.M., Uyar, A.,
627 O'rourke, R., O'rourke, S., Ingraham, C., Bednarczyk, D., Belanger, M., Cope, Z.A., Little,
628 G.J., Williams, S.G., Ash, C., Bleckert, A., Ragan, T., Logsdon, B.A., Mangravite, L.M.,
629 Sukoff Rizzo, S.J., Territo, P.R., Carter, G.W., Howell, G.R., Sasner, M., and Lamb, B.T.
630 (2021). Comprehensive Evaluation of the 5XFAD Mouse Model for Preclinical Testing
631 Applications: A MODEL-AD Study. *Front Aging Neurosci* 13**,** 713726.
632 Onos, K.D., Quinney, S.K., Jones, D.R., Masters, A.R., Pandey, R., Keezer, K.J., Biesdorf, C.,
633 Metzger, I.F., Meyers, J.A., Peters, J., Persohn, S.C., Mccarthy, B.P., Bedwell, A.A.,
634 Figueiredo, L.L., Cope, Z.A., Sasner, M., Howell, G.R., Williams, H.M., Oblak, A.L., Lamb,
635 B.T., Carter, G.W., Rizzo, S.J.S., and Territo, P.R. (2022). Pharmacokinetic,
636 pharmacodynamic, and transcriptomic analysis of chronic levetiracetam treatment in

637 5XFAD mice: A MODEL-AD preclinical testing core study. *Alzheimers Dement (N Y)* 8**,**
638 e12329.
639 Palop, J.J. (2009). Epilepsy and Cognitive Impairments in Alzheimer Disease. *Archives of*
640 *Neurology* 66**,** 435.
641 Palop, J.J., Chin, J., Roberson, E.D., Wang, J., Thwin, M.T., Bien-Ly, N., Yoo, J., Ho, K.O., Yu,
642 G.-Q., Kreitzer, A., Finkbeiner, S., Noebels, J.L., and Mucke, L. (2007). Aberrant
643 Excitatory Neuronal Activity and Compensatory Remodeling of Inhibitory Hippocampal
644 Circuits in Mouse Models of Alzheimer's Disease. *Neuron* 55**,** 697-711.
645 Paxinos, G., and Keith B. J. Franklin, M. (2007). *The Mouse Brain in Stereotaxic Coordinates.*
646 Elsevier Science.
647 Percie Du Sert, N., Ahluwalia, A., Alam, S., Avey, M.T., Baker, M., Browne, W.J., Clark, A.,
648 Cuthill, I.C., Dirnagl, U., Emerson, M., Garner, P., Holgate, S.T., Howells, D.W., Hurst, V.,
649 Karp, N.A., Lazic, S.E., Lidster, K., Maccallum, C.J., Macleod, M., Pearl, E.J., Petersen,
650 O.H., Rawle, F., Reynolds, P., Rooney, K., Sena, E.S., Silberberg, S.D., Steckler, T., and
651 Wurbel, H. (2020). Reporting animal research: Explanation and elaboration for the
652 ARRIVE guidelines 2.0. *PLoS Biol* 18**,** e3000411.
653 Preuss, C., Pandey, R., Piazza, E., Fine, A., Uyar, A., Perumal, T., Garceau, D., Kotredes, K.P.,
654 Williams, H., Mangravite, L.M., Lamb, B.T., Oblak, A.L., Howell, G.R., Sasner, M.,
655 Logsdon, B.A., Consortium, M.-A., and Carter, G.W. (2020). A novel systems biology
656 approach to evaluate mouse models of late-onset Alzheimer's disease. *Mol*
657 *Neurodegener* 15**,** 67.
658 Sanchez, P.E., Zhu, L., Verret, L., Vossel, K.A., Orr, A.G., Cirrito, J.R., Devidze, N., Ho, K., Yu,
659 G.-Q., Palop, J.J., and Mucke, L. (2012). Levetiracetam suppresses neuronal network
660 dysfunction and reverses synaptic and cognitive deficits in an Alzheimer’s disease model.
661 *Proceedings of the National Academy of Sciences* 109**,** E2895-E2903.

662 Schneider, F., Baldauf, K., Wetzel, W., and Reymann, K.G. (2014). Behavioral and EEG
663 changes in male 5xFAD mice. *Physiol Behav* 135**,** 25-33.
664 Sensini, F., Inta, D., Palme, R., Brandwein, C., Pfeiffer, N., Riva, M.A., Gass, P., and Mallien,
665 A.S. (2020). The impact of handling technique and handling frequency on laboratory
666 mouse welfare is sex-specific. *Scientific Reports* 10.
667 Stafstrom, C.E. (2005). The role of the subiculum in epilepsy and epileptogenesis. *Epilepsy Curr*
668 5**,** 121-129.
669 Surges, R., Volynski, K.E., and Walker, M.C. (2008). Review: Is levetiracetam different from
670 other antiepileptic drugs? Levetiracetam and its cellular mechanism of action in epilepsy
671 revisited. *Therapeutic Advances in Neurological Disorders* 1**,** 13-24.
672 Team, R.C. (2023). "_R: A Language and Environment for Statistical Computing_.". 4.3.0 ed.
673 (Vienna, Austria: R Foundation for Statistical Computing).
674 Toniolo, S., Sen, A., and Husain, M. (2020). Modulation of Brain Hyperexcitability: Potential New
675 Therapeutic Approaches in Alzheimer's Disease. *Int J Mol Sci* 21.
676 Tran, T.T., Speck, C.L., Pisupati, A., Gallagher, M., and Bakker, A. (2017). Increased
677 hippocampal activation in ApoE-4 carriers and non-carriers with amnestic mild cognitive
678 impairment. *Neuroimage Clin* 13**,** 237-245.
679 Veronese, M., Moro, L., Arcolin, M., Dipasquale, O., Rizzo, G., Expert, P., Khan, W., Fisher,
680 P.M., Svarer, C., Bertoldo, A., Howes, O., and Turkheimer, F.E. (2019). Covariance
681 statistics and network analysis of brain PET imaging studies. *Scientific Reports* 9.
682 Vossel, K., Ranasinghe, K.G., Beagle, A.J., La, A., Ah Pook, K., Castro, M., Mizuiri, D., Honma,
683 S.M., Venkateswaran, N., Koestler, M., Zhang, W., Mucke, L., Howell, M.J., Possin, K.L.,
684 Kramer, J.H., Boxer, A.L., Miller, B.L., Nagarajan, S.S., and Kirsch, H.E. (2021). Effect of
685 Levetiracetam on Cognition in Patients With Alzheimer Disease With and Without
686 Epileptiform Activity. *JAMA Neurology* 78**,** 1345.

687 Vossel, K.A., Ranasinghe, K.G., Beagle, A.J., Mizuiri, D., Honma, S.M., Dowling, A.F., Darwish,
688 S.M., Van Berlo, V., Barnes, D.E., Mantle, M., Karydas, A.M., Coppola, G., Roberson,
689 E.D., Miller, B.L., Garcia, P.A., Kirsch, H.E., Mucke, L., and Nagarajan, S.S. (2016).
690 Incidence and impact of subclinical epileptiform activity in Alzheimer's disease. *Annals of*
691 *Neurology* 80**,** 858-870.
692 Wan, Y.-W., Al-Ouran, R., Mangleburg, C.G., Perumal, T.M., Lee, T.V., Allison, K., Swarup, V.,
693 Funk, C.C., Gaiteri, C., Allen, M., Wang, M., Neuner, S.M., Kaczorowski, C.C., Philip,
694 V.M., Howell, G.R., Martini-Stoica, H., Zheng, H., Mei, H., Zhong, X., Kim, J.W., Dawson,
695 V.L., Dawson, T.M., Pao, P.-C., Tsai, L.-H., Haure-Mirande, J.-V., Ehrlich, M.E.,
696 Chakrabarty, P., Levites, Y., Wang, X., Dammer, E.B., Srivastava, G., Mukherjee, S.,
697 Sieberts, S.K., Omberg, L., Dang, K.D., Eddy, J.A., Snyder, P., Chae, Y., Amberkar, S.,
698 Wei, W., Hide, W., Preuss, C., Ergun, A., Ebert, P.J., Airey, D.C., Mostafavi, S., Yu, L.,
699 Klein, H.-U., Carter, G.W., Collier, D.A., Golde, T.E., Levey, A.I., Bennett, D.A., Estrada,
700 K., Townsend, T.M., Zhang, B., Schadt, E., De Jager, P.L., Price, N.D., Ertekin-Taner, N.,
701 Liu, Z., Shulman, J.M., Mangravite, L.M., and Logsdon, B.A. (2020). Meta-Analysis of the
702 Alzheimer’s Disease Human Brain Transcriptome and Functional Dissection in Mouse
703 Models. *Cell Reports* 32**,** 107908.
704 Wang, M., Beckmann, N.D., Roussos, P., Wang, E., Zhou, X., Wang, Q., Ming, C., Neff, R., Ma,
705 W., Fullard, J.F., Hauberg, M.E., Bendl, J., Peters, M.A., Logsdon, B., Wang, P., Mahajan,
706 M., Mangravite, L.M., Dammer, E.B., Duong, D.M., Lah, J.J., Seyfried, N.T., Levey, A.I.,
707 Buxbaum, J.D., Ehrlich, M., Gandy, S., Katsel, P., Haroutunian, V., Schadt, E., and
708 Zhang, B. (2018). The Mount Sinai cohort of large-scale genomic, transcriptomic and
709 proteomic data in Alzheimer's disease. *Scientific Data* 5**,** 180185.
710 Xiang, X., Wind, K., Wiedemann, T., Blume, T., Shi, Y., Briel, N., Beyer, L., Biechele, G.,
711 Eckenweber, F., Zatcepin, A., Lammich, S., Ribicic, S., Tahirovic, S., Willem, M.,

712 Deussing, M., Palleis, C., Rauchmann, B.S., Gildehaus, F.J., Lindner, S., Spitz, C.,
713 Franzmeier, N., Baumann, K., Rominger, A., Bartenstein, P., Ziegler, S., Drzezga, A.,
714 Respondek, G., Buerger, K., Perneczky, R., Levin, J., Hoglinger, G.U., Herms, J., Haass,
715 C., and Brendel, M. (2021). Microglial activation states drive glucose uptake and FDG-
716 PET alterations in neurodegenerative diseases. *Sci Transl Med* 13**,** eabe5640.
717